DOI: 10.1002/ adfm.201802803
Article type: Full Paper

Title: Interplay of structural and optoelectronic properties in formamidinium mixed tin-lead triiodide perovskites

*Elizabeth S. Parrott, Thomas Green, Rebecca L. Milot, Michael B. Johnston, Henry J. Snaith, Laura M. Herz**

E. S. Parrott, T. Green, Dr. R. L. Milot, Prof. M. B. Johnston, Prof. H. J. Snaith, Prof. L. M. Herz
Department of Physics, University of Oxford, Clarendon Laboratory, Parks Road, Oxford OX1 3PU, UK
E-mail: laura.herz@physics.ox.ac.uk

Keywords: perovskite solar cells, photoluminescence, band-gap bowing, recombination

Mixed lead-tin triiodide perovskites are promising absorber materials for low band-gap bottom cells in all-perovskite tandem photovoltaic devices. Key structural and electronic properties of the $FAPb_{1-x}Sn_xI_3$ perovskite are presented here as a function of lead:tin content across the alloy series. Temperature-dependent photoluminescence and optical absorption measurements are used to identify changes in the band-gap and phase transition temperature. The large band-gap bowing parameter, a crucial element for the attainment of low band-gaps in this system, is shown to depend on the structural phase, reaching a value of 0.84 eV in the low-temperature phase and 0.73 eV at room temperature. The parabolic nature of the bowing at all temperatures is compatible with a mechanism arising from bond bending to accommodate the random placement of unevenly sized lead and tin ions. Charge-carrier recombination dynamics are shown to fall into two regimes. Tin-rich compositions exhibit fast, mono-exponential recombination that is almost temperature independent, in accordance with high levels of electrical doping. Lead-rich compositions show slower, stretched-exponential charge-carrier recombination that is strongly temperature-dependent, in accordance with a multi-phonon assisted process. These results highlight the importance of structure and composition for control of band-gap bowing and charge-carrier recombination mechanisms in low band-gap absorbers for all-perovskite tandem solar cells.

1. Introduction

Metal-halide perovskites (ABX_3) are a type of solution processable yet highly crystalline semiconductor with high charge-carrier mobilities[1] and a direct optical band-gap[2], showing promise for applications in solar cells with record power conversion efficiencies (PCEs) currently nearing that of crystalline silicon.[3] In addition to single-junction solar cells, all-perovskite tandem cells have been developed with a record 4-terminal efficiency[4] of 23% and 2-terminal efficiency[5] of 18.5%. These achievements have been enabled by the widely tuneable band-gap of mixed perovskites extending from 1.2 to 3.0 eV through alloying of the metal cation (Pb^{2+}, Sn^{2+}),[6,7] A-cation ($HC(NH_2)_2^+$ (FA), $CH_3NH_3^+$ (MA), Cs^+)[8–10] and halide (I^-, Br^-, Cl^-).[10–14] The benefit of tandem or multi-junction solar cells is that they employ two or more semiconducting materials absorbing different portions of the solar spectrum, thus reducing charge thermalization losses and enabling a higher PCE than is possible for a single-junction cell.[15] Since a significant proportion of the overall cost of solar panels is made up of installation, structural and land costs, all of which scale with area, high efficiency solar cells are important in reducing the resultant price of electricity.[16] However, tandem cells are typically expensive to make, offsetting the benefit of their higher efficiencies to energy prices[17] and limiting their application. A perovskite tandem solar cell which retains the low-cost production of solution-processable materials whilst achieving the efficiency boost enabled by multiple layers therefore has great potential to deliver large scale and affordable renewable energy.[18]

To achieve the highest efficiencies, tandem solar cells require a narrow band-gap semiconductor of around 0.8-1.2 eV to absorb the infrared portion of the solar spectrum.[18] To obtain such a low band-gap from a metal halide perovskite, one may utilize the interesting phenomenon of band-gap bowing observed when lead and tin perovskites are alloyed.[6] In contrast to the linear change in band-gap observed for metal halide perovskites with compositional changes in A-cation[8] and halide anion[12], alloyed lead-tin perovskites have

been found to exhibit lower band-gaps than either of the 'parent' compositions $APbX_3$ or $ASnX_3$. It is common for semiconductor alloys to display some degree of band-gap bowing, with the band-gap bowing parameter *b* being defined by the following equation:[19]

$$E(x) = E_1 x + E_2 (1-x) + b\, x\, (1-x) \quad (1)$$

where $E(x)$ is the band-gap energy of the mixed composition comprising material 1 with band-gap energy E_1 and material 2 with band-gap energy E_2, and x is the proportion of material 1. The first two terms represent a linear change in band gap with composition between the two end points, and the third term captures a quadratic deviation from linearity. Equation 1 shows that a maximum deviation ΔE occurs at x=0.5 and is given by $\Delta E = b/4$ (see Figure 2a). There is little understanding of the cause of band-gap bowing in metal halide perovskites at the present time, and reports disagree on both the origin[7,20] and magnitude of the effect. Hao[6], Zhao[21], Anaya[22] and Liu[23] all report bowing in $MAPb_{1-x}Sn_xI_3$ with a minimum band-gap of just below 1.2 eV at around 80% tin fraction, determined from optical absorbance or EQE measurements. Yang[24] reports a minimum of 1.27 eV at 75% tin, Im[20] and Stoumpos[25] find a minimum band-gap of 1.1eV at around 50% tin content, while Ogami finds the minimum band-gap to be 1.1eV at 100% tin with little bowing. For $FAPb_{1-x}Sn_xI_3$, Eperon[7] and Prasanna[9] report a minimum band-gap of 1.2 and 1.25 eV respectively at around 60% tin content. Clearly if these materials are to be optimised for tandem devices, a greater understanding and control of the factors influencing the band-gap are required.

Aside from the band-gap, other properties of the mixed perovskites are important in determining how the material will perform in a photovoltaic (PV) cell, namely the charge-carrier lifetimes and PL quantum efficiencies. Lifetimes must be sufficiently long for carriers to be extracted before they recombine, and non-radiative recombination pathways must be minimised to reach maximum efficiencies. All-perovskite tandem solar cells are limited in part by the poorer performance of perovskite materials containing tin.[7] For $MASnI_3$, poor device performance has been linked to very fast charge-carrier recombination, largely as a

result of spontaneous p-doping due to the formation of defects such as tin vacancies.[26–28] However the presence of spontaneous doping in mixed metal perovskites is less clear as there are only a handful of reports of charge recombination lifetimes for mixed metal perovskites in the literature to date. $(FASn)_{0.6}(MAPb)_{0.4}I_3$ is shown to have a PL lifetime intermediate to that of $FASnI_3$ and $MAPbI_3$.[29] From optical pump terahertz probe spectroscopy the monomolecular and bimolecular recombination rates for $FASn_{0.5}Pb_{0.5}I_3$ also take intermediate values compared to values for 100% Sn or Pb reported elsewhere in the literature.[7] Zhao *et al.* show that metal composition has an impact on charge recombination mechanisms in $MAPb_{1-x}Sn_xI_3$, with 20-40% Sn having much weaker photoluminescence than other compositions, and all tin-rich compositions having short PL lifetimes.[21] They show that the dominant recombination mechanism at low intensity is Shockley-Read-Hall (SRH) recombination, but that at high intensity, the 60% Sn composition, which gives highest device efficiency, becomes dominated by radiative recombination (as determined from the diode ideality factor).[21] To reduce SRH recombination, a defect passivating electron transport layer can be used, which has been shown to increase device efficiency for $MASn_{0.5}Pb_{0.5}I_3$.[5] Finally, increasing film crystallinity and thickness is reported to increase the lifetime by an order of magnitude[4]. The charge-carrier lifetimes and recombination mechanisms of $FAPb_{1-x}Sn_xI_3$ have not yet been systematically studied as a function of metal composition, although FA has been shown to be a good choice of cation in mixed tin-lead perovskites, improving stability[24] and PL lifetime,[30] and supporting single-junction PV devices that currently achieve PCEs of around 15%.[7,29]

In response to the broad lack of knowledge regarding these device-relevant materials, we investigate the optoelectronic properties of $FAPb_{1-x}Sn_xI_3$, through photoluminescence and optical absorption measurements across the Pb-Sn spectrum at temperatures from 5 to 300 K. We highlight several key properties important for the improvement of mixed-metal halide perovskites and provide fundamental insights, through experiment and by drawing on the

wealth of literature on traditional inorganic semiconductors. We report the structural phase transition temperatures as a function of composition, and show that the phase influences the magnitude of the bowing parameter and the gradient of the band-gap with temperature. We show that the charge-carrier recombination dynamics can be split into two regimes – fast, mono-exponential recombination with a higher proportion of radiative recombination for tin-rich compositions and slower, stretched-exponential recombination for the lead-rich compositions. We also demonstrate that the charge recombination rate is almost temperature independent for $FASnI_3$, whereas there is strongly temperature activated non-radiative recombination in $FAPb_{0.75}Sn_{0.25}I_3$, which we attribute to multi-phonon assisted charge-carrier recombination.

2. Results and Discussion

2.1. Temperature-dependence of the band-gap

We first explore the general behaviour of the band-gap with temperature, for several compositions with varying tin content. We observed discontinuities in the PL and absorption edge for all compositions which we ascribe to phase transitions, similar to what has been seen in other hybrid perovskite materials.[31,32] **Figure 1**a and 1b highlight this discontinuity for the 45% Sn (x=0.45) composition on color maps of the PL and the reflection-corrected absorption spectrum respectively, at temperatures between 5 and 295 K (see Figure S1 for color maps for different compositions). Figure 1c shows how the phase transition temperature changes with composition. The transitions of the end compositions agree with those reported in the literature, from PL[32] and X-ray diffraction[33] measurements for 100% lead and resistivity measurements for 100% tin[34]. Our results show that the transition temperature changes linearly with tin fraction between these end points. Further to the transitions in Figure 1c, we see a second discontinuity, only in $FASnI_3$, which may indicate a further phase transition at

170 K. This could correspond to the Pnma (orthorhombic) to P4/mbm (tetragonal) transition reported at around 150 K by Schueller *et al*.[35] Schueller also reports a transition to a cubic structure at 250 K which from our results appears to have no influence on the PL. Comparing the other transitions with those reported in literature, $FAPbI_3$ is thought to be in a trigonal space group at low temperature, with a gentle transition to another trigonal space group, beginning at 100 K and completing at 175 K on heating,[32,33] which is in accordance with our results. Across the compositions at room temperature there is thought to be a structural change from the space group P3m1 (trigonal) for lead rich compositions to Amm2 (orthorhombic) for tin rich compositions[36,37], in the region of 25% tin.[7] However, in other studies $FASnI_3$ has been reported to have cubic structure ($Pm\bar{3}m$) at room temperature,[35] including in single crystals.[34,38]

Apart from the discontinuities at the phase transitions, the band-gap changes linearly with temperature. For all compositions, we observed that both the PL maximum and absorption onset blue-shift as the temperature is increased, implying an increasing band-gap, as has been observed for all other metal halide perovskite semiconductors[26,31,39,40]. This finding is contrary to the usual behaviour of semiconductors for which the band-gap decreases as the temperature increases (negative dE_g/dT), according to the empirical Varshni formula.[41] Although one might intuitively expect this decrease (red-shift) as the lattice expands, in fact the lattice expansion is usually a relatively small contribution, and can increase or decrease the band-gap with temperature as determined by detailed band structure calculations.[42] The main contribution to the change in band-gap with temperature is the influence of phonons i.e. the change in band-gap caused by the dynamic displacement of atoms due to thermal lattice vibrations (rather than the phonon anharmonicity responsible for lattice expansion).[43] Phonons usually reduce the band-gap as the temperature is raised, but can increase it, and there can be multiple phonons with opposite effects on the band-gap in the same material, resulting in complex temperature dependence.[44] For metal halide perovskites it was initially

proposed that the linear increase in band-gap with increasing temperature is due to the cancellation of phonon terms with opposite effect on the band-gap, leaving lattice expansion as the dominant contribution.[39] More recently, calculations have shown that the phonon anharmonicity is large, possibly making the lattice expansion explanation plausible without the need for other terms cancelling.[45] As the lattice constant is increased, the valance band maximum decreases linearly because of the reduced overlap of the Pb-6s and I-5s antibonding orbitals, therefore increasing the band-gap.[46] However another study has identified that the Pb-I-Pb bond bending phonon mode increases the band-gap and suggests this to be the main contribution.[47]

Figure 1d shows the gradient of the band-gap with respect to temperature in the highest and lowest temperature phase (as determined from linear fits to Figure S3). In the room temperature phase, the band-gap of the 100% tin composition is the most sensitive to temperature (steepest gradient) and 100% lead the least, with the gradients of the mixed compositions linearly interpolating between the two. However, in the low temperature phase the gradient is smallest for the 65 and 85% Sn compositions. The phonon modes are thought to be relatively constant in the different phases of $FAPbI_3$,[40] and our results show the temperature gradient is also the same in both phases measured. The tin-containing compositions all have different values of the temperature gradient for the two phases, which may indicate that the phonon modes are also different. It is also worth noting that the minimum gradient in the low temperature phase coincides with the minimum band-gap energy and seems to approximately follow the bowing in **Figure 2**a. If the main contribution to the temperature dependence of the band-gap is in fact lattice expansion, this could suggest hindered thermal expansion in the mixed compositions, possibly as a result of local strain to accommodate the different metal ions, which is also a factor that causes band-gap bowing.

2.2 Changes in band-gap bowing with temperature

Given that both the structure and the temperature influence the band-gap, it is interesting to investigate how the bowing is affected. To determine the band-gap bowing parameter *b*, we fit Equation 1 to the absorption onset energy across the 6 compositions at a given temperature. Example fits are shown in Figure 2a for high and low temperature. We confirm that there is significant band-gap bowing, with the middle compositions having lower energy than the pure compositions, across all temperatures. Band-gap bowing has sometimes also been referred to as an 'anomalous' band-gap, but we stress that it is simply the result of the generally applicable equation for semiconductor band-gaps (Equation 1), for a large value of *b*. Metal halide perovskites are essentially crystalline semiconductors, therefore we consider it informative for us to make a comparison with other materials that display band-gap bowing. For traditional inorganic semiconductors it is true that the bowing parameter *b* is usually small compared to the size of the band-gap,[48] with only slight deviation from the linear behaviour often referred to as 'Vegard's Law',[49] which was however originally stated for lattice parameters rather than band-gaps. There are however a handful of semiconductors with bowing parameters large enough for the mixed compositions to have lower band-gaps than either of the end compositions, including GaN_xAs_{1-x}, $GaAs_xSb_{1-x}$, $CdSe_xTe_{1-x}$ and ZnS_xTe_{1-x}.[48,50] Here, the band-gap bowing is thought to be caused by the local environment around the alloyed atom, meaning that averaging the properties of the alloy atoms (the 'Virtual Crystal Approximation') is not valid. Extended X-ray absorption fine structure (EXAFS) measurements show that for pseudo-binary alloys such as those we have listed, the individual bond lengths are often closer to those of the un-alloyed materials, rather than adopting an intermediate value. The mismatch resulting from the different sizes of the alloyed atoms is then accommodated by local changes to bond angles, which results in properties that cannot be described by considering the global structure where the bond lengths take an average value and the angles are all the same. [51,52] In perovskites the bond angles, specifically the tilting of the octahedra, have been shown to be important in determining the band-gap[20,53] and may

provide a rationale for the large bowing parameter. These effects can be calculated using density functional theory (DFT), but since the local placement of the atoms is important, large supercells are required, making it computationally expensive to model. DFT has been used to calculate bowing in $FAPb_{1-x}Sn_xI_3$ for a 2x2x2 supercell with some success despite the small size.[7] However, more in-depth calculations are required to allow for a full understanding of such effects in hybrid metal halide perovskites.

In certain cases (usually where the size or electronegativity of the alloy atoms differ greatly from each other) band-gap bowing can be described by considering an atom as an impurity that forms a new localised energy level which, if sufficiently close in energy, mixes with the conduction or valence band to form two new bands[54]. The bowing can then be modelled by a simple 'band anti-crossing' (BAC) equation,[54] interpolated between the two impurity limits[55] and in some cases producing highly non-parabolic bowing.[56] We note however that our data are well represented by the parabolic model of bowing at all temperatures. It is therefore unlikely that the band anti-crossing model of bowing is applicable here, since this characteristically results in highly non-parabolic bowing, with a sudden drop in band-gap at one end of the composition range, which we do not observe for the tin-lead perovskites at any composition or temperature.

To determine the effect of temperature on band-gap bowing, we extract the bowing parameter *b* from both PL and absorption data, as shown in Figure 2b as a function of temperature. In the shaded temperature region, individual compositions undergo phase transitions at different temperature, with the corresponding jump in band-gap leading to strong fluctuations of the extracted bowing parameter. However, outside of this intermediate range, we observe a roughly constant bowing parameter in both the low temperature region (~0–70K) and the high temperature region (~170–300K) within which no phase transitions occur. Absorption data indicate a bowing parameter of 0.73 eV for the high temperature phase

and 0.84 eV for the low temperature phase (see also Figure S15) highlighting the influence of crystal structure on the extent of band-gap bowing.

We note that the bowing calculated from PL measurements is higher than that calculated from the absorption onsets but the data converge at 5 K. These discrepancies can be understood by consideration of the changes in Stokes shift with temperature, shown in Figure S4. At room temperature, the PL peak energy will exhibit stronger bowing than at low temperature (5K) because of the larger Stokes shift for the alloyed compositions. Similarly, it has been previously found for InGaN that PL measurements gave an overestimated bowing parameter, as a result of the larger Stokes Shift of mixed compositions.[57] The absorption edge, as we have measured it, should be minimally affected by alloy disorder and therefore provides a more accurate value of the band-gap bowing parameter.

Overall, we conclude that band-gap bowing in tin-lead perovskites is likely to arise from bond bending to accommodate the random placement of lead and tin ions, given the parabolic nature of the large bowing we observe for all temperatures. The bowing parameter is largely constant with temperature for regions in which all compositions do not exhibit structural phase transitions. However, crystal structure clearly has an effect on the magnitude of the bowing parameter, possibly through its influence on bond angles, suggesting that small structural changes, e.g. through A-cation choice, may be used to optimize desired bowing effects.

2.3 Changes in emission spectra with tin-lead composition

We proceed by considering the influence of composition on disorder and PL quantum efficiency, which are highly important parameters for optimized power conversion efficiency of solar cells. For this purpose, we investigate the PL and absorption spectra at room temperature for 12 compositions with varying tin content (0, 6.25, 12.5, 25, 37.5, 50, 62.5, 75, 81.25, 87.5, 93.75 and 100 %).

2.3.1. Spectral broadening

The PL linewidth data (**Figure 3**a) show that the 100% tin and 100% lead iodide perovskites have much sharper PL spectra than those of their alloys, indicating higher disorder for mixed metal compositions. This observation is in agreement with the model discussed above, which assumes that random placement of tin and lead atoms on metal sites in the perovskite lattice is the main cause of band-gap bowing effects. From intuition and previous DFT calculations[7], we would expect the linewidth to be broadest for the 50% composition, whereas in fact we find the broadest linewidth in the mixed compositions with Sn <25% and >85%. Since many material quality factors affect material disorder, this effect is likely to arise from extrinsic factors that can be improved with further crystal growth optimisation, such as ensuring there are no inclusions of the yellow δ-phase in the lead-rich compositions.[7,58] Interestingly the PL linewidth of $FASnI_3$ is similar to that of $FAPbI_3$, and much narrower than that observed previously for $MASnI_3$[26] suggesting that $FASnI_3$, (as prepared here with excess SnF_2) may be less disordered and therefore able to support higher device efficiencies than its MA equivalent.

2.3.2. Stokes Shift

The Stokes shift between emission peak and absorption edge is found to rise steeply when tin is added, then drops again and stays approximately constant for 40-100% tin content (Figure 3b). The large Stokes shift for materials with 6-12% Sn content suggests that a significant fraction of the PL originates from sub-band-gap states that exist in a severely disordered or defected material. Potential explanations could be a re-alignment of the level of trap states with respect to band edges as a small quantity of tin is added, or a structural instability (e.g. deterioration into a δ-phase) causing an energetically disordered landscape. Particle size effects can also contribute to a change in Stokes Shift for crystal sizes on the order of 10nm and below,[59] but since the thickness and grain size for our films are in the 100-500nm range[7], we do not expect to see this effect.

2.3.3. Quantum Efficiency

The PL quantum efficiency (PLQE) is of particular interest for solar cell applications because the presence of non-radiative recombination in the semiconductor implies there will be detrimental recombination in the photovoltaic device; therefore a higher PLQE of an absorber material will generally allow for higher PCEs. Here we examine relative PLQE values by dividing the luminescence intensity by the excitation power, across the tin-lead composition range. Figure 3c shows that the relative PLQE drops by almost 2 orders of magnitude when only 6% tin is added to $FAPbI_3$, but then rises exponentially as the tin content is increased. The sudden drop in PLQE for small additions of tin may have similar causes to those leading to the large Stokes shift for these compositions, e.g. an unfavourable re-alignment of trap levels or increase in their density, or an increase in energetic disorder. As we show in section 2.4.1, the subsequent rise in PLQE with increasing tin content above 50% can be mainly understood in the context of an increased density of background holes present caused by spontaneous doping, which has been associated with the propensity of the material to form Sn vacancies[28,60]. As a result, $FASnI_3$ has the highest PLQE in the series, being 10 times brighter than $FAPbI_3$.

2.4 Charge-carrier recombination dynamics

Charge-carrier recombination processes compete with charge extraction in working solar cells. To investigate how such mechanisms are affected by composition in mixed-lead iodide perovskites, we acquired PL transients for a range of different temperatures and excitation fluences. The following rate equation is often used in the literature[1,27,61–63] to describe the time-dependence of a photo-generated charge-carrier density Δn:

$$\frac{d(\Delta n)}{dt} = -k_1^{nr}\Delta n - k_2^r(p_0 + \Delta n).\Delta n$$

$$= -(k_1^{nr} + k_1^r)\Delta n - k_2^r\Delta n^2 \quad (2)$$

Here, k_1^{nr} is the monomolecular non-radiative recombination rate that typically reflects trap-mediated Shockley-Read-Hall recombination, k_2^r is the bimolecular radiative recombination rate constant, and p_0 is the non-intrinsic background hole density present in the dark as a result of doping. Previous studies have shown significant contributions from a monomolecular radiative rate $k_1^r = p_0 k_2^r$, attributed to the recombination of photogenerated electrons with holes arising from doping.[61] Equation 2 inherently captures the dependence of the measured decay transients on the fluence of the initial excitation pulse. For low fluences, a mono-exponential decay with time constant $(k_1^{nr} + k_1^r)^{-1}$ is expected, while at higher fluences, bi-molecular decay kinetics lead to accelerated, non-exponential dynamics. However, as we argue below, Shockley-Read-Hall recombination does not necessarily always lead to mono-exponential decay dynamics even in the low fluence regime, either because of a spatially uneven trap distribution, or the nature of the trap levels. We therefore choose instead to parameterize the decay curves with a stretched exponential $I = I_0 \exp(-[t/\tau]^{\beta})$ and extract $\tau_{eff,}$ the effective lifetime and β, the stretch parameter.

2.4.1. PL transients as a function of tin-lead composition

Figure 4 demonstrates that the charge-carrier recombination kinetics fall into two distinct compositional regions: a lead rich region with Sn<50% that exhibits stretched decay curves (β<1) and longer lifetimes, and a tin rich region with mono-exponential decay curves (β=1) and short lifetimes. Since the tin rich compositions have reduced lifetimes, we can conclude that their higher PLQE is caused by a relative increase in radiative recombination rate, rather than a decrease in non-radiative recombination rate. A survey of the literature values reveals that the apparent radiative bimolecular recombination constant k_2 is twice as large for $FASnI_3$[61] than $FAPbI_3$[64], with an intermediate value for a composition with 50% Sn[7]. Therefore, an enhancement in radiative recombination for tin-rich samples could be partly accounted for by enhanced band-to-band recombination. However, such effects cannot fully account for the order of magnitude rise in PLQE between the lead and tin perovskites. We

therefore attribute the increased luminescence of the tin-rich compositions to enhanced radiative recombination mediated by hole doping, an explanation which is consistent with Hall measurements[65,66] and other techniques[27,61] that have reported high doping densities for various tin-based perovskites, although such effects may be reduced substantially through suitable processing methods.[37,38]

In addition, analysis of the stretch-parameter β (Figure 4c) can yield interesting insights into the mechanisms for charge recombination. As we show below, the non-radiative recombination rate for a fluence of 14 nJ cm^{-2} exceeds the radiative rate by at least a factor 100 across all compositions at room temperature and hence it is the trap-mediated recombination that will determine the dynamics. The non-radiative recombination of charge-carriers in semiconductors is generally described by the Shockley-Read-Hall (SRH) model.[67] For many cases, the common assumption of a constant decay rate k_1 (as in Equation 2) is a good approximation to SRH recombination, applicable to many situations such as extrinsically doped semiconductors, and leads to mono-exponential decay dynamics. However the full SRH formula has a more complex dependence on the photoexcited carrier density Δn that can result in non-exponential charge-carrier decay, e.g. for the case of intrinsic semiconductors with shallow traps (see Equation S7 and discussion in the SI). Non-exponential PL decay is also possible when the PL dynamics are determined by trap-filling rather than trap-assisted recombination (see SI Section 3.3).[68,69] For lead triiodide perovskites, theoretical calculations have previously found the typical defect states to be very shallow[70] and the doping level to be intrinsic[71], which is consistent with the stretched-exponential behaviour we observe for the lead-rich compositions. Hence the transition to mono-exponential decays for tin-rich compositions could be caused either by the substantial increase in doping density that we have already proposed, or by an increase in trap depth.

Overall, our observation of two distinct regimes for the stretch-parameter β suggests that there is a substantial change in the nature of defect formation at around 50% Sn. Based on the enhanced PLQE and shorter lifetimes for high tin content, this change is likely to cause or be accompanied by a change in doping density. A recent study investigating the stability of $FAPb_{1-x}Sn_xI_3$ showed that compositions with less than 50% Sn were far more air-stable than tin-rich compositions, as a result of two different degradation mechanisms dominating in the two different regimes.[72] Although we did not intentionally expose our samples to air during either fabrication or measurement, spontaneous defect formation would follow similar thermodynamic considerations. Hence a switch in the nature of the defects between tin rich (x>0.5) and lead rich perovskites (x<0.5) is also the most likely explanation for the change in the shape of the decay transients we observe here.

2.4.2. PL transients as a function of temperature

To allow for an identification of trap-mediated charge-carrier recombination mechanisms, we investigate the temperature dependence of the PL dynamics. PL transients (**Figure 5**c and Figures S8 & S9) were measured for three compositions (25, 87.5 and 100% Sn) at temperatures between 5 and 295 K for low and high fluences of 14 nJ cm^{-2} and 1400 nJ cm^{-2}. Figures 5a and 5b show example values of the extracted effective PL lifetimes as a function of temperature for the 25% and 100% Sn perovskites, with further data shown in Figure S10.

We find that the effective PL lifetime increases with decreasing temperature for all compositions investigated, but more so for the tin-poor samples than for the 100% Sn perovskite whose PL lifetimes show only weak dependence on temperature. To investigate whether such effects are the result of changes in radiative or non-radiative decay pathways, we also recorded the relative PL quantum efficiencies as a function of temperature, shown in Figure 5d. The observed strong increase in relative PLQE for the 25% Sn perovskite with decreasing temperature indicates that the concomitant increase in PL lifetime is mostly related to a decrease in the non-radiative (trap-mediated) recombination rate (k_1^{nr} in Equation 2).

Similar observations have previously been made for $MAPbI_3$ for which k_1 was shown to decrease upon cooling,[31] and for $FAPbI_3$ where the PLQE was shown to have a similarly strong temperature dependence.[32]

We note that higher radiative efficiencies at lower temperature may also result from an increase in the radiative bimolecular recombination rate constant k_2 with decreasing temperature. Such trends would be expected, as such band-to-band recombination has recently been shown to be the inverse process to absorption (by the principle of detailed balance) and therefore the enhancement at low temperature is caused by the sharpening of the photon and charge carrier distribution functions.[2] We do indeed find that the PL lifetimes reduce (k_2 higher) at low temperature (<60 K), where such radiative band-to-band recombination begins to play a larger role, evidenced by the higher PLQE. The difference in high and low excitation lifetimes in this temperature region also supports the larger role of k_2 . However, if it were the dominant process across all temperatures at the excitation fluences used, we would expect PL lifetimes to decrease with decreasing temperature, which is not observed. We therefore conclude, in agreement with our arguments above, that non-radiative trap-mediated processes are the primary cause of the increased lifetime and PLQE as temperature is decreased, and dominate the charge-carrier recombination processes at room temperature here.

To understand the temperature dependence of these trap-mediated charge-carrier recombination processes we consider several mechanisms within the theory of Shockley-Read-Hall recombination. The rate of SRH recombination (or alternatively of trap filling, see SI section 3.3) depends on charge carrier densities and on the lifetimes of the trapped electrons and holes (see SI section 3.2 for a detailed discussion). The temperature dependence of the charge-carrier densities can be calculated from Fermi-Dirac statistics – the densities reduce as the temperature is lowered. The SRH lifetimes, corresponding to the rates at which electrons and holes are trapped, are determined by the physical mechanism of recombination and can therefore display a variety of temperature dependent behaviours. For clarity we will

discuss the mechanisms in terms of electron trapping, but the mechanisms are equivalent for hole trapping. The most common mechanism in traditional semiconductors is multi-phonon recombination, during which a trapped electron moves to a lower energy level by converting its energy into several phonons.[73] There is an activation energy associated with this process because energy and momentum conservation requires a number of particular phonons to be absorbed, in addition to those emitted.[74] The temperature dependence of the process depends on conditions such as the charge of the trap, whether the transition is between localised states or bands, and the possibility for quantum tunnelling through the energy barrier, but in all cases the rate is expected to increase with temperature according to a power law or exponential rise, which has indeed been observed in experiments.[75] An alternative mechanism is cascade capture, where a charged trap has hydrogen-like excited states that an electron can cascade through by emitting a single phonon each time.[76] In contrast to the multi-phonon process, the rate decreases with increasing temperature, since the electron is more likely to be thermally excited out of the first level.[75,76] The recombination rate is also expected to decrease in the presence of a continuous distribution of traps for the same reason.[77,78] As another channel (though one not included in the simple SRH model), trap-assisted Auger recombination may operate, during which an electron loses its energy to another electron.[79] Trap-assisted Auger recombination is only weakly dependent on temperature.[79] Finally, an electron can emit a photon when it is captured, which would contribute to the PL spectrum at an energy lower than the band-gap. This process is also weakly dependent on temperature, but tends to be slower than the other mechanisms.[75]

With this knowledge of trap-mediated recombination processes in mind, we therefore conclude that the strongly temperature-activated non-radiative recombination channels in the 25% perovskite are most likely the result of multi-phonon assisted SRH recombination. Fits to the relative PLQE yield an upper limit to the activation energy of around 40 meV for this process (see SI section 2.2 for details). However to obtain a better fit at low temperature, an

additional term must be included, which may be due either to the temperature dependence of radiative recombination[2] or to the presence of a distribution of traps, which is only distinguishable at low temperature, as proposed recently for $FAPbI_3$.[78] However, we note that such fits also have an uncertainty because they do not take photon reabsorption into account.[80]

As Figure 5b and 5d illustrate, the 100% tin composition exhibits significantly less temperature-activated behaviour, with PL lifetimes and relative PLQE only rising slightly with decreasing temperature. These data therefore suggest that, in $FASnI_3$, either trap-assisted Auger recombination or multi-phonon SRH recombination with a very small activation energy (0.5 meV from the fit in Fig 5d) is the predominant mechanism in operation. These are both non-radiative processes, accounting for the low relative PLQE. However, as discussed above, the SRH model predicts a trap-mediated mono-exponential decay (β=1) of charge-carrier densities in the presence of high doping levels, whereas trap-assisted Auger recombination does not,[79] making an SRH mechanism the most likely non-radiative recombination process to be in action for $FASnI_3$ here. In contrast to what is observed for the 25% Sn composition, the PL lifetimes at high and low fluence are very similar at room temperature, and only show a small difference at low temperature. This is unsurprising given the large value of k_1 indicated by the rapid monoexponential decay, meaning a very high fluence (much higher than the maximum of 1400 nJ cm^{-2} used here) is needed to reach the carrier densities required to observe significant bimolecular recombination. We note also that for all compositions, we do not see any direct evidence of trap saturation, which could result in an increase in lifetime at higher fluence. To summarize our findings for the charge-carrier recombination channels in $FAPb_{1-x}Sn_xI_3$, we have shown that non-radiative pathways dominate for all compositions at room temperature at a fluence of 14 nJ cm^{-2}. The lead-rich composition with 25% Sn has a temperature-activated non-radiative recombination pathway indicative of multi-phonon recombination. In contrast, charge recombination channels in

$FASnI_3$ (100% Sn) are hardly affected by temperature. We find that at room temperature the PL decay dynamics fall into a lead-rich regime with longer lifetimes and stretched exponential decays, and a tin-rich regime with shorter lifetimes and mono-exponential decays. These observations are in agreement with a previous study showing that decomposition pathways, and hence defect formation, differ substantially in the tin- and lead-rich composition regimes.[72] We discussed that Shockley-Read-Hall statistics predict fluence-dependent charge-carrier recombination for intrinsic semiconductors, but fluence-independent mono-exponential behaviour for heavily doped semiconductors, which underpins the difference in recombination dynamics we observe for these two regimes. Doping also enhances radiative recombination which, even if it is not the dominant mechanism in recombination dynamics, still increases the PLQE by an order of magnitude for $FASnI_3$ in comparison to $FAPbI_3$.

3. Conclusion

In conclusion, we have demonstrated the important influence of composition and temperature on the band-gap and recombination mechanisms of $FAPb_{1-x}Sn_xI_3$, two essential properties in the design of efficient solar cells. We have reported structural phase transition temperatures for mixed compositions for the first time and a band-gap bowing parameter of 0.73 and 0.84 eV for the room temperature and low temperature phases respectively, showing that crystal structure influences the magnitude of bowing. We have used a combination of temperature dependent transient PL and PLQE measurements to distinguish different recombination mechanisms, showing that there is still considerable non-radiative recombination at room temperature in both 25 and 100% Sn compositions. This strongly suggests that efforts to increase lifetimes of tin-rich perovskites should focus not only on controlling doping densities but also on reducing non-radiative recombination via trap states. For our range of compositions of $FAPb_{1-x}Sn_xI_3$ we find the perovskite with around 40% Sn to be the most promising low band-gap material for use in tandem solar cells. $FAPb_{0.6}Sn_{0.4}I_3$

combines the long charge-carrier lifetime of the lead-rich materials with a PLQE approaching that of $FAPbI_3$ and a relatively small Stokes shift and PL linewidth compared to the other alloys. Its band-gap of around 1.3 eV is suitable for tandem devices and fairly close to the minimum achievable for $FAPb_{1-x}Sn_xI_3$ alloys. However, our work highlights that the optoelectronic properties of these materials are still highly dominated by extrinsic effects. Therefore, more favourable properties may still be obtained across the series with additional materials engineering, such as the optimisation of treatments with compounds such as SnF_2 to increase the charge carrier lifetime of the tin-rich compositions or addition of other cations and halides to tune the structural properties, which will influence both the band-gap bowing and the charge-carrier lifetimes. Our study highlights the link between such structural and optoelectronic properties, thus paving a way towards more guided materials design.

4. Experimental Section

Sample preparation: $FAPb_{1-x}Sn_xI_3$ perovskite thin films were formed on z-cut quartz disks by spin-coating precursor solutions of $FASnI_3$ and $FAPbI_3$ in appropriate ratios. The precursor solutions were prepared at a concentration of 1M in a mixed solvent of DMF:DMSO 65:35 by volume. The solutions were dissolved at a 1:1 molar ratio of formamidinium iodide ($HC(NH_2)_2I$) to tin iodide (SnI_2) or lead iodide (PbI_2). In addition, excess SnF_2 (0.2M) was added into the $FASnI_3$ precursor (i.e. providing a 20% excess of tin). The Sn and Pb containing solutions were then mixed in the appropriate ratio before spin-coating at 5000 rpm in a nitrogen-filled glovebox. After dropping the solution onto the spinning substrate the speed was ramped down to zero (~5 seconds). The wet transparent film was then immediately immersed into a small petri dish containing anisole (~5s) and blow-dried with a nitrogen gun. Anisole was not used for the 45 and 65% Sn samples which were spin-coated for 12s including a ramp up (~6s), blow-dried with a nitrogen-gun whilst still spinning for 16s, spin-coated for a further 8s followed by a ramp down (~5s) which obtained uniform film coverage. A comparison of the films made with and without anisole for 87.5% Sn is found in Figure S11. The reddish or transparent precursor films were then annealed at 70°C for 20 minutes. For the pure Pb and 6.25% Sn films, annealing at 170°C for 10 minutes and 1 minute respectively was necessary to form the black phase perovskite as it formed the yellow phase when heated only at 70°C. Tin halide perovskites are known to easily degrade in air, and the

tin-rich compositions turned visibly transparent within hours or days (see also our previous results for samples fabricated in the same way[7]). For this reason, all samples were fabricated inside a nitrogen filled glovebox and mounted in a vacuum chamber or sealed cryostat whilst still inside the glovebox to eliminate exposure to air. The chamber/cryostat was then transferred to the laser laboratory and evacuated, maintaining a pressure below 10^{-5} mbar during measurements. This was effective at preventing degradation, as shown e.g. by our repeated measurements of a sample with 87.5% tin content, giving the same results when measured at the beginning and end of a 2-month time interval.

Photoluminescence spectra: To control the temperature, the sample was mounted in a cold-finger cryostat (MicrostatHe, Oxford Instruments). The temperature was controlled by a flow of liquid helium and an electronic temperature controller (ITC503, Oxford Instruments). The temperature was monitored with sensors both on the cryostat heat exchanger and the end of the sample holder. Samples were excited with the aid of a tunable Ti:Sapphire pulsed (80 fs) laser, with its fundamental wavelength set to 800 nm and an 80 MHz repetition rate (Mai Tai, Spectra-Physics). A BBO crystal was used to double the excitation frequency, giving an excitation wavelength of 400 nm. The 800 nm fundamental wavelength was filtered out using a polarizer and a color filter. The excitation intensity was attenuated using an OD1 filter and a variable attenuator consisting of a waveplate and a vertical polariser to achieve 1 mW or 100 mW over a beam size of 0.09 mm^2, giving fluences of 14 or 1400 nJ/cm^2., corresponding to charge carrier densities on the order of 10^{15} and 10^{17} respectively. A horizontal polariser and a 550-nm long-pass color filter were placed after the sample to remove any laser scatter from the spectrum. Photoluminescence from the sample was collected by a pair of off-axis parabolic mirrors and focused onto the entry slit of a grating monochromator (Triax, Horiba). The spectrally resolved PL was detected by a nitrogen-cooled Si-CCD detector (Symphony, Horiba) and the spectral response of all components was corrected for using a tungsten filament lamp with known spectrum. This is particularly important for tin perovskites since the sensitivity of the CCD drops off in the NIR where these materials emit.

Transient photoluminescence: The set up for time-resolved photoluminescence for the compositions with Sn<50% was the same as above, except that light emitted at the peak PL wavelength was selected by a second slit and detected by a silicon single photon avalanche diode used for time correlated single photon counting (TCSPC). The instrument response function was measured by tuning the (80-fs pulsed) laser to the wavelength of the

luminescence for each sample (since the detector response is slightly dependent on detection wavelength), and measuring the response due to laser scatter from a roughened quartz disk placed in the sample holder. The excitation powers used were 1 mW and 100 mW over a beam size of 0.09 mm^2 pulsed at 80 MHz, giving fluences of 14 and 1400 $nJ\,cm^{-2}$.

For the compositions with Sn ≥ 50%, the decay time was too long for the pulse window. Instead an electronically pulsed diode laser with variable pulse frequency (PicoHarp LDH-D-C-405M) was used for excitation, the wavelength was selected using Princeton Instruments SP-2558 grating spectrometer before detection by a silicon single photon avalanche diode. The excitation power was chosen to match the fluence (14 and 1400 $nJ\,cm^{-2}$) over a beam size of 0.018 mm^2 for various pulse rates between 0.5 and 20 MHz.

Optical Absorption: Samples were mounted in a helium gas exchange cryostat to control the temperature, with the same set-up for temperature control as the PL measurements. However, due to the configuration of the system, the samples had to be exposed to air for about a minute during transfer before being measured under vacuum.

Visible to near infrared (NIR) transmission and reflection measurements were performed using a Fourier transform infrared spectrometer (Vertex 80v, Bruker). A tungsten halogen lamp was used as a light source, and the light passing through the sample (T) and reflected from the sample (R) was detected by a nitrogen cooled InSb detector (NIR) and a silicon diode detector (visible). A blank substrate and a silver mirror were used as references for 100% transmission and reflection respectively. Background measurements were also used to correct for any scatter from the sample holder and other optical components. The absorbance was calculated from the measured transmission and reflection (equation S1). The absorption edge was defined as the point on the absorption curve with the steepest gradient, and was found by differentiation of the curve in the region of the absorption onset. This definition will give a slightly larger energy than that determined by a Tauc Plot, but we prefer this method since the exciton enhancement of the band edge[81] makes the Tauc Plot reading unphysical, and may be part of the reason for the wide range of band-gap energies reported (see SI section 2.1 for more details).

Supporting

Supporting Information is available from the Wiley Online Library or from the author.

Acknowledgements

The authors acknowledge the Engineering and Physical Sciences Research Council (EPSRC) and the EU Horizon 2020 Programme (INFORM ITN Grant No. 675867) for financial support. E.S.P. thanks the EPSRC Centre for Doctoral Training in New and Sustainable Photovoltaics (CDT-PV) for support through a doctoral studentship.

Received: ((will be filled in by the editorial staff))
Revised: ((will be filled in by the editorial staff))
Published online: ((will be filled in by the editorial staff))

References

[1] L. M. Herz, *ACS Energy Lett.* **2017**, *2*, 1539.

[2] C. L. Davies, M. R. Filip, J. B. Patel, T. W. Crothers, C. Verdi, A. D. Wright, R. L. Milot, F. Giustino, M. B. Johnston, L. M. Herz, *Nat. Commun.* **2018**, *9*, 293.

[3] W. S. Yang, B.-W. Park, E. H. Jung, N. J. Jeon, Y. C. Kim, D. U. Lee, S. S. Shin, J. Seo, E. K. Kim, J. H. Noh, S. Il Seok, *Science (80-.).* **2017**, *356*, 1376.

[4] D. Zhao, Y. Yu, C. Wang, W. Liao, N. Shrestha, C. R. Grice, A. J. Cimaroli, L. Guan, R. J. Ellingson, K. Zhu, X. Zhao, R.-G. Xiong, Y. Yan, *Nat. Energy* **2017**, *2*, 17018.

[5] A. Rajagopal, Z. Yang, S. B. Jo, I. L. Braly, P. W. Liang, H. W. Hillhouse, A. K. Y. Jen, *Adv. Mater.* **2017**, *29*, 1.

[6] F. Hao, C. C. Stoumpos, R. P. H. H. Chang, M. G. Kanatzidis, *J. Am. Chem. Soc.* **2014**, *136*, 8094.

[7] G. E. Eperon, T. Leijtens, K. A. Bush, R. Prasanna, T. Green, D. P. Wang, Jacob Tse-Wei Mcmeekin, G. Volonakis, R. L. Milot, R. May, A. Palmstrom, D. J. Slotcavage, R. A. Belisle, J. B. Patel, E. S. Parrott, R. J. Sutton, W. Ma, F. Moghadam, B. Conings, A. Babayigit, H. Boyen, S. Bent, F. Giustino, L. M. Herz, M. B. Johnston, M. D. McGehee, H. J. Snaith, *Science (80-.).* **2016**, *364*, 861.

[8] O. J. Weber, B. Charles, M. T. Weller, *J. Mater. Chem. A* **2016**, *4*, 15375.

[9] R. Prasanna, A. Gold-Parker, T. Leijtens, B. Conings, A. Babayigit, H. G. Boyen, M. F. Toney, M. D. McGehee, *J. Am. Chem. Soc.* **2017**, *139*, 11117.

[10] W. Rehman, D. P. McMeekin, J. B. Patel, R. L. Milot, M. B. Johnston, H. J. Snaith, L.

M. Herz, *Energy Environ. Sci.* **2017**, *10*, 361.

[11] G. Xing, N. Mathews, S. S. Lim, N. Yantara, X. Liu, D. Sabba, M. Grätzel, S. Mhaisalkar, T. C. Sum, *Nat. Mater.* **2014**, *13*, 476.

[12] J. H. Noh, S. H. Im, J. H. Heo, T. N. Mandal, S. Il Seok, *Nano Lett.* **2013**, *13*, 1764.

[13] G. E. Eperon, S. D. Stranks, C. Menelaou, M. B. Johnston, L. M. Herz, H. J. Snaith, *Energy Environ. Sci.* **2014**, *7*, 982.

[14] R. J. Sutton, G. E. Eperon, L. Miranda, E. S. Parrott, B. A. Kamino, J. B. Patel, M. T. Hörantner, M. B. Johnston, A. A. Haghighirad, D. T. Moore, H. J. Snaith, *Adv. Energy Mater.* **2016**, 1502458.

[15] A. De Vos, *J. Phys. D. Appl. Phys.* **1980**, *13*, 839.

[16] M. T. Hörantner, T. Leijtens, M. E. Ziffer, G. E. Eperon, M. G. Christoforo, M. D. McGehee, H. J. Snaith, *ACS Energy Lett.* **2017**, *2*, 2506.

[17] S. Essig, C. Allebé, T. Remo, J. F. Geisz, M. A. Steiner, K. Horowitz, L. Barraud, J. S. Ward, M. Schnabel, A. Descoeudres, D. L. Young, M. Woodhouse, M. Despeisse, C. Ballif, A. Tamboli, *Nat. Energy* **2017**, *2*, 17144.

[18] G. E. Eperon, M. T. Hörantner, H. J. Snaith, *Nat. Rev. Chem.* **2017**, *1*, 95.

[19] J. A. Van Vechten, T. K. Bergstresser, *Phys. Rev. B* **1970**, *1*, 3351.

[20] J. Im, C. C. Stoumpos, H. Jin, A. J. Freeman, M. G. Kanatzidis, *J. Phys. Chem. Lett.* **2015**, *6*, 3203.

[21] B. Zhao, M. Abdi-Jalebi, M. Tabachnyk, H. Glass, V. S. Kamboj, W. A. Nie, J. Pearson, Y. Puttisong, K. C. Gödel, H. E. Beere, D. A. Ritchie, A. D. Mohite, S. E. Dutton, R. H. Friend, A. Sadhanala, *Adv. Mater.* **2016**, *29*, 1604744.

[22] M. Anaya, J. P. Correa-Baena, G. Lozano, M. Saliba, P. Anguita, B. Roose, A. Abate, U. Steiner, M. Grätzel, M. E. Calvo, A. Hagfeldt, H. Míguez, *J. Mater. Chem. A* **2016**, *4*, 11214.

[23] C. Liu, J. Fan, H. Li, C. Zhang, Y. Mai, A. Kojima, K. Teshima, Y. Shirai, T. Miyasaka,

J. H. Im, C. R. Lee, J. W. Lee, S. W. Park, N. G. Park, J. Burschka, M. Liu, M. B. Johnston, H. J. Snaith, H. Zhou, W.-S. Yang, D. Bi, M. A. Green, A. Ho-Baillie, H. J. Snaith, G. Hodes, D. Cahen, G. Niu, F. Hao, C. C. Stoumpos, R. P. Chang, M. G. Kanatzidis, Y. Ogomi, F. Zuo, A. Babayigit, A. Ethirajan, M. Muller, B. Conings, A. Babayigit, F. Hao, C. C. Stoumpos, D. H. Cao, R. P. H. Chang, M. G. Kanatzidis, N. K. Noel, F. Hao, S. J. Lee, W. Li, J. Fan, J. Li, Y. Mai, L. Wang, Q. Chen, Y. C. Kim, C. Liu, S. D. Stranks, G. Xing, H. S. Kim, *Sci. Rep.* **2016**, *6*, 35705.

[24] Z. Yang, A. Rajagopal, C. Chueh, S. B. Jo, B. Liu, T. Zhao, A. K. Jen, *Adv. Mater.* **2016**, *28*, 8990.

[25] C. C. Stoumpos, M. G. Kanatzidis, *Acc. Chem. Res.* **2015**, *48*, 2791.

[26] E. S. Parrott, R. L. Milot, T. Stergiopoulos, H. J. Snaith, M. B. Johnston, L. M. Herz, *J. Phys. Chem. Lett.* **2016**, *7*, 1321.

[27] N. K. Noel, S. D. Stranks, A. Abate, C. Wehrenfennig, S. Guarnera, A. Haghighirad, A. Sadhanala, G. E. Eperon, S. K. Pathak, M. B. Johnston, A. Petrozza, L. Herz, H. Snaith, *Energy Environ. Sci.* **2014**, *7*, 3061.

[28] Y. Y. Takahashi, R. Obara, Z.-Z. Lin, Y. Y. Takahashi, T. Naito, T. Inabe, S. Ishibashi, K. Terakura, *Dalton Trans.* **2011**, *40*, 5563.

[29] W. Liao, D. Zhao, Y. Yu, N. Shrestha, K. Ghimire, C. R. Grice, C. Wang, Y. Xiao, A. J. Cimaroli, R. J. Ellingson, N. J. Podraza, K. Zhu, R. G. Xiong, Y. Yan, *J. Am. Chem. Soc.* **2016**, *138*, 12360.

[30] Z. Zhao, F. Gu, Y. Li, W. Sun, S. Ye, H. Rao, Z. Liu, Z. Bian, C. Huang, *Adv. Sci.* **2017**, 1700204.

[31] R. L. Milot, G. E. Eperon, H. J. Snaith, M. B. Johnston, L. M. Herz, *Adv. Funct. Mater.* **2015**, *25*, 6218.

[32] H. Fang, F. Wang, S. Adjokatse, N. Zhao, J. Even, M. A. Loi, *Light Sci. Appl.* **2016**, *5*, e16056.

[33] T. Chen, B. J. Foley, C. Park, C. M. Brown, L. W. Harriger, J. Lee, J. Ruff, M. Yoon, J. J. Choi, S.-H. Lee, *Sci. Adv.* **2016**, *2*, e1601650.

[34] D. B. Mitzi, K. Liang, *J. Solid State Chem.* **1997**, *381*, 376.

[35] E. C. Schueller, G. Laurita, D. H. Fabini, C. C. Stoumpos, M. G. Kanatzidis, R. Seshadri, *Inorg. Chem.* **2018**, *57*, 695.

[36] T. M. Koh, T. Krishnamoorthy, N. Yantara, C. Shi, W. L. Leong, P. P. Boix, A. C. Grimsdale, S. G. Mhaisalkar, N. Mathews, *J. Mater. Chem. A* **2015**, *3*, 14996.

[37] C. C. Stoumpos, C. D. Malliakas, M. G. Kanatzidis, *Inorg. Chem.* **2013**, *52*, 9019.

[38] Y. Dang, Y. Zhou, X. Liu, D. Ju, S. Xia, H. Xia, X. Tao, *Angew. Chemie - Int. Ed.* **2016**, *55*, 3447.

[39] C. Yu, Z. Chen, J. Wang, W. Pfenninger, N. Vockic, J. T. Kenney, K. Shum, *J. Appl. Phys.* **2011**, *110*, 63526.

[40] A. D. Wright, C. Verdi, R. L. Milot, G. E. Eperon, M. A. Pérez-Osorio, H. J. Snaith, F. Giustino, M. B. Johnston, L. M. Herz, *Nat. Commun.* **2016**, *7*, 11755.

[41] Y. P. Varshni, *Physica* **1967**, *34*, 149.

[42] P. B. Allen, V. Heine, *J. Phys. C Solid State Phys.* **1976**, *9*, 2305.

[43] H. Y. Fan, *Phys. Rev.* **1951**, *82*, 900.

[44] A. Göbel, T. Ruf, M. Cardona, C. T. Lin, J. Wrzesinski, M. Steube, K. Reimann, J.-C. Merle, M. Joucla, *Phys. Rev. B* **1998**, *57*, 15183.

[45] L. D. Whalley, J. M. Skelton, J. M. Frost, A. Walsh, *Phys. Rev. B* **2016**, *94*, 220301(R).

[46] M. I. Dar, G. Jacopin, S. Meloni, A. Mattoni, N. Arora, A. Boziki, S. M. Zakeeruddin, U. Rothlisberger, M. Gratzel, *Sci. Adv.* **2016**, *2*, e1601156.

[47] H. Kim, J. Hunger, E. Cánovas, M. Karakus, Z. Mics, M. Grechko, D. Turchinovich, S. H. Parekh, M. Bonn, *Nat. Commun.* **2017**, *8*, 687.

[48] I. Vurgaftman, J. R. Meyer, L. R. Ram-Mohan, *J. Appl. Phys.* **2001**, *89*, 5815.

[49] L. Vegard, *Zeitschrift fur Phys.* **1921**, *5*, 17.

[50] I. Hernandez-Calderon, In *II VI Semiconductor Materials and Their Applications*; Tamargo, M. C., Ed.; Taylor and Francis New York, 2002; pp. 113–170.

[51] C. S. Schnohr, *Appl. Phys. Rev.* **2015**, *2*, 31304.

[52] J. B. Boyce, J. C. Mikkelsen, *J. Cryst. Growth* **1989**, *98*, 37.

[53] A. Amat, E. Mosconi, E. Ronca, C. Quarti, P. Umari, M. K. Nazeeruddin, M. Grätzel, F. De Angelis, *Nano Lett.* **2014**, *14*, 3608.

[54] W. Shan, W. Walukiewicz, J. Ager, E. Haller, J. Geisz, D. Friedman, J. Olson, S. Kurtz, *Phys. Rev. Lett.* **1999**, *82*, 1221.

[55] J. Wu, W. Shan, W. Walukiewicz, *Semicond. Sci. Technol.* **2002**, *17*, 860.

[56] K. M. Yu, S. V. Novikov, R. Broesler, A. X. Levander, Z. Liliental-Weber, F. Luckert, R. W. Martin, O. Dubon, J. Wu, W. Walukiewicz, C. T. Foxon, *Phys. Status Solidi C* **2011**, *8*, 2503.

[57] J. Wu, W. Walukiewicz, K. M. Yu, J. W. Ager, E. E. Haller, H. Lu, W. J. Schaff, *Appl. Phys. Lett.* **2002**, *80*, 4741.

[58] Z. Li, M. Yang, J. S. Park, S. H. Wei, J. J. Berry, K. Zhu, *Chem. Mater.* **2016**, *28*, 284.

[59] M. C. Brennan, J. Zinna, M. Kuno, *ACS Energy Lett.* **2017**, *2*, 1487−1488.

[60] I. Chung, J. H. Song, J. Im, J. Androulakis, C. D. Malliakas, H. Li, A. J. Freeman, J. T. Kenney, M. G. Kanatzidis, *J. Am. Chem. Soc.* **2012**, *134*, 8579.

[61] R. L. Milot, G. E. Eperon, T. Green, H. J. Snaith, M. B. Johnston, L. M. Herz, *J. Phys. Chem. Lett.* **2016**, *7*, 4178.

[62] R. L. Milot, R. J. Sutton, G. E. Eperon, A. A. Haghighirad, J. Martinez Hardigree, L. Miranda, H. J. Snaith, M. B. Johnston, L. M. Herz, *Nano Lett.* **2016**, *16*, 7001.

[63] J. M. Richter, M. Abdi-Jalebi, A. Sadhanala, M. Tabachnyk, J. P. H. Rivett, L. M. Pazos-Outón, K. C. Gödel, M. Price, F. Deschler, R. H. Friend, *Nat. Commun.* **2016**, *7*, 13941.

[64] W. Rehman, R. L. Milot, G. E. Eperon, C. Wehrenfennig, J. L. Boland, H. J. Snaith, M.

B. Johnston, L. M. Herz, *Adv. Mater.* **2015**, *27*, 7938.

[65] Y. Y. Takahashi, H. Hasegawa, Y. Y. Takahashi, T. Inabe, *J. Solid State Chem.* **2013**, *205*, 39.

[66] D. Sabba, H. K. Mulmudi, R. R. Prabhakar, T. Krishnamoorthy, T. Baikie, P. P. Boix, S. G. Mhaisalkar, N. Mathews, *J. Phys. Chem. C* **2015**, *119*, 1763.

[67] W. Shockley, W. T. Read, *Phys. Rev.* **1952**, *87*, 835.

[68] S. D. Stranks, V. M. Burlakov, T. Leijtens, J. M. Ball, A. Goriely, H. J. Snaith, *Phys. Rev. Appl.* **2014**, *2*, 34007.

[69] G. K. Wertheim, *Phys. Rev.* **1958**, *109*, 1086.

[70] J. Kim, S.-H. Lee, J. H. Lee, K.-H. Hong, *J. Phys. Chem. Lett.* **2014**, *5*, 1312.

[71] J. Huang, Y. Yuan, Y. Shao, Y. Yan, *Nat. Rev. Mater.* **2017**, *2*, 17042.

[72] T. Leijtens, R. Prasanna, A. Gold-Parker, M. F. Toney, M. D. McGehee, *ACS Energy Lett.* **2017**, *2*, 2159.

[73] R. N. Hall, *Proc. IEE - Part B Electron. Commun. Eng.* **1959**, *106*, 923.

[74] A. Alkauskas, Q. Yan, C. G. Van De Walle, *Phys. Rev. B - Condens. Matter Mater. Phys.* **2014**, *90*, 1.

[75] V. L. Bonch-Bruevich, E. G. Landsberg, *Phys. Status Solidi* **1968**, *29*, 9.

[76] M. Lax, *J. Phys. Chem. Solids* **1959**, *8*, 66.

[77] D. Monroe, *Phys. Rev. Lett.* **1985**, *54*, 146.

[78] A. D. Wright, R. L. Milot, G. E. Eperon, H. J. Snaith, M. B. Johnston, L. M. Herz, *Adv. Funct. Mater.* **2017**, *27*, 1700860.

[79] D. J. Robbins, P. T. Landsberg, *J. Phys. C Solid State Phys.* **1980**, *13*, 2425.

[80] T. W. Crothers, R. L. Milot, J. B. Patel, E. S. Parrott, J. Schlipf, P. Müller-Buschbaum, M. B. Johnston, L. M. Herz, *Nano Lett.* **2017**, *17*, 5782.

[81] R. J. Elliott, *Phys. Rev.* **1957**, *108*, 1384.

[82] G. Kieslich, S. Sun, T. Cheetham, *Chem. Sci.* **2015**, *6*, 3430.

[83] S. G. Motti, M. Gandini, A. J. Barker, J. M. Ball, A. R. Srimath Kandada, A. Petrozza, *ACS Energy Lett.* **2016**, *1*, 726.

[84] T. Bin Song, T. Yokoyama, C. C. Stoumpos, J. Logsdon, D. H. Cao, M. R. Wasielewski, S. Aramaki, M. G. Kanatzidis, *J. Am. Chem. Soc.* **2017**, *139*, 836.

[85] M. A. Green, A. Ho-Baillie, H. J. Snaith, *Nat. Photonics* **2014**, *8*, 506.

[86] M. Leroux, N. Grandjean, B. Beaumont, G. Nataf, F. Semond, J. Massies, P. Gibart, *Phys. Status Solidi Basic Res.* **1999**, *216*, 605.

[87] S. Sun, T. Salim, N. Mathews, M. Duchamp, C. Boothroyd, G. Xing, T. C. Sum, Y. M. Lam, *Energy Environ. Sci.* **2014**, *7*, 399.

[88] T. J. Savenije, C. S. Ponseca, L. Kunneman, M. Abdellah, K. Zheng, Y. Tian, Q. Zhu, S. E. Canton, I. G. Scheblykin, T. Pullerits, A. Yartsev, V. Sundstro, *J. Phys. Chem. Lett.* **2014**, *5*, 2189.

[89] K. Wu, A. Bera, C. Ma, Y. Du, Y. Yang, L. Li, T. Wu, *Phys. Chem. Chem. Phys.* **2014**, *16*, 22476.

[90] A. Miyata, A. Mitioglu, P. Plochocka, O. Portugall, J. T.-W. Wang, S. D. Stranks, H. J. Snaith, R. J. Nicholas, *Nat. Phys.* **2015**, *11*, 582.

[91] T. Leijtens, G. Eperon, A. Barker, G. Grancini, W. Zhang, J. Ball, A. R. Srimath Kandada, H. Snaith, A. Petrozza, *Energy Environ. Sci.* **2016**, *9*, 3472.

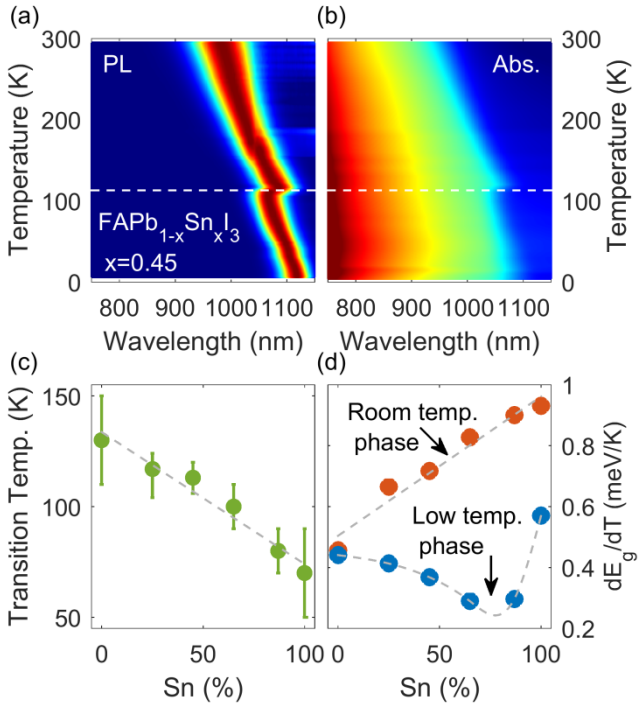

Figure 1. Example of a color map of (a) PL intensity (excited at 400 nm, 1 W cm^{-2}) and (b) absorption coefficient of $FAPb_{1-x}Sn_xI_3$, showing spectra taken at different temperatures with intervals of 5 K. The identified phase transition is shown by the dashed white line. (c) Lowest temperature phase transition for each tin composition, found from the discontinuity in PL and absorption edge energies when heating the sample from 4 K to room temperature. The error bars indicate the temperature range over which the discontinuity is found. (d) Gradient of the absorption edge with respect to temperature for each composition in its room temperature phase and lowest temperature phase.

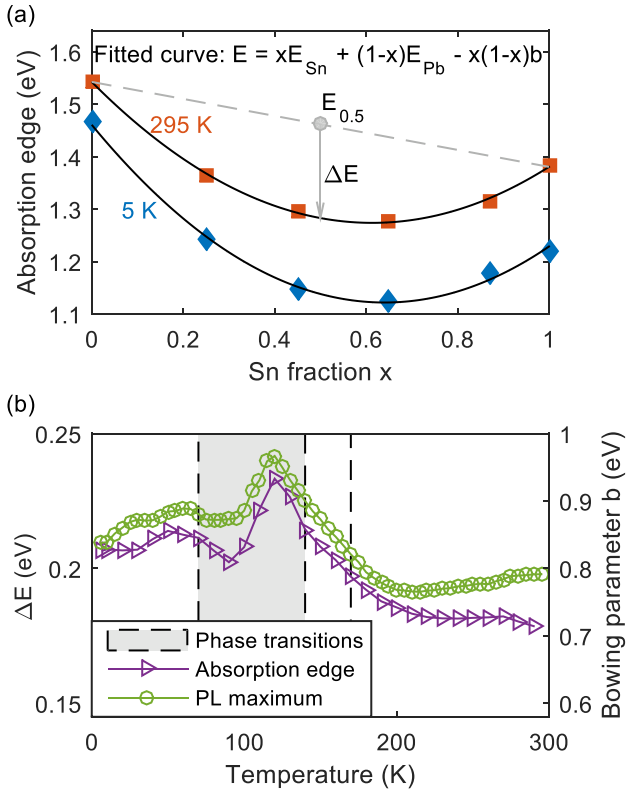

Figure 2. (a) Absorption edge of $FAPb_{1-x}Sn_xI_3$ at high (red squares) and low (blue diamonds) temperature. Black lines show fitted parabolas that determine the bowing parameter *b*. The dashed line shows the expected energies if the band-gap changed linearly, and ΔE is the maximum deviation from linear (always at 50% Sn), which equals *b*/4. (b) Bowing parameter calculated from fitting a parabola to the absorption edge energy (purple triangles), and the energy of maximum PL intensity (green circles) of all compositions, at each temperature. The shaded area shows the temperature region in which the phase transitions of the different compositions occur, and the dashed line is the extra phase transition of $FASnI_3$. For PL spectra, we excited the samples with a pulsed laser at 400 nm with a fluence of 14 $nJcm^{-2}$ and collected spectra at intervals of 5 K.

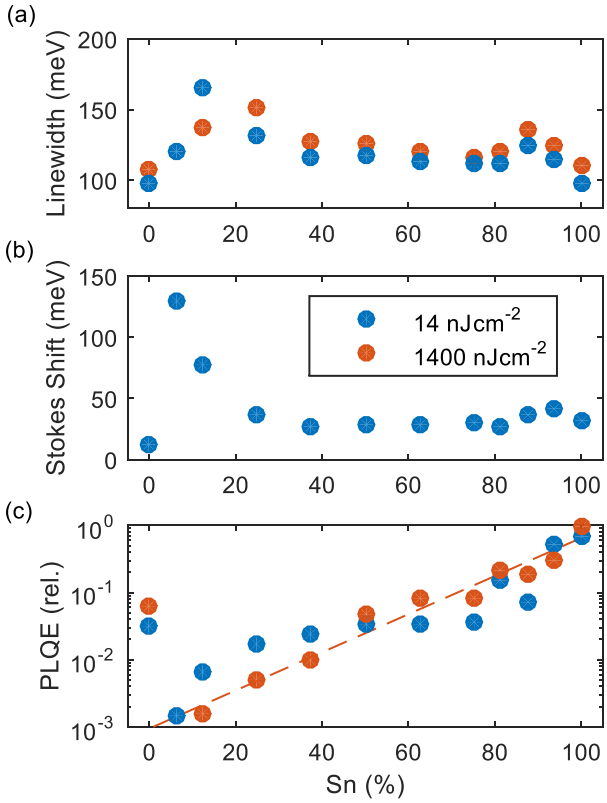

Figure 3. (a) Full width at half maximum of the PL spectrum for each composition of $FAPb_{1-x}Sn_xI_3$, excited at 400 nm with a fluence of 14 nJ cm^{-2} (blue) and 1400 nJ cm^{-2} (red). (b) Stokes shift of the same compositions determined by the difference between the absorption edge and the PL peak (400 nm, 14 nJ cm^{-2}). (c) Relative photoluminescence quantum efficiency (PLQE) for the same compositions, excited at 400 nm with a fluence of 14 nJ cm^{-2} (blue) and 1400 nJ cm^{-2} (red). The PLQE is normalized to the value for 100% Sn, measured at 1400 nJ cm^{-2} fluence.The dashed line shows an exponential fit to the high fluence data, excluding the 0% Sn point.

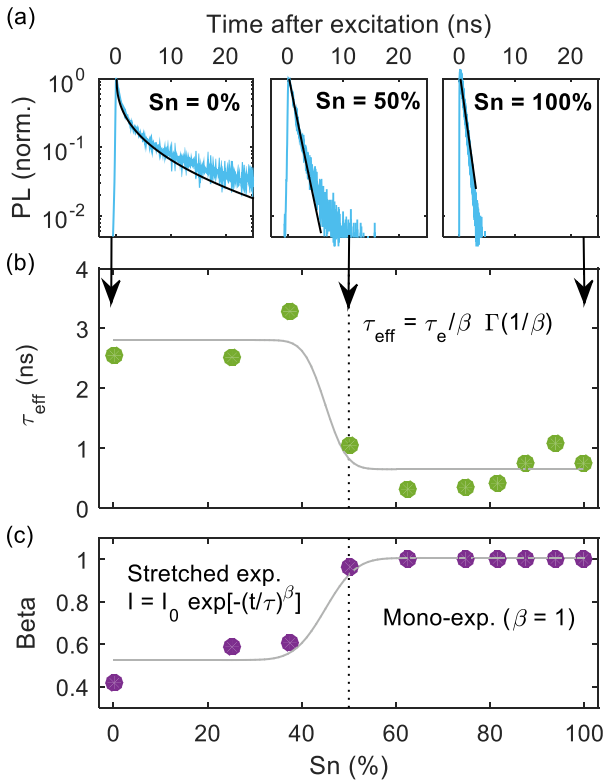

Figure 4. (a) Example PL decay curves (blue) of $FAPb_{1-x}Sn_xI_3$ compositions at room temperature when excited at 400nm with 14 nJ/cm^2 excitation power, fitted (black) with a stretched exponential ($I = I_0 \exp(-(t/\tau)^{\beta})$), where beta is the stretch parameter. The rest are shown in Figure S6. From these fits, (b) shows the PL effective lifetime ($\tau_{eff} = \tau/\beta\ \Gamma(1/\beta)$ where Γ is the gamma function) and (c) the stretch parameter. Perovskites containing only 6.25 and 12.5% Sn were too weakly luminescent to be measured at this excitation intensity, but could be examined at a higher excitation intensity for which they also exhibit a long PL lifetime and stretched decay (Figure S7).

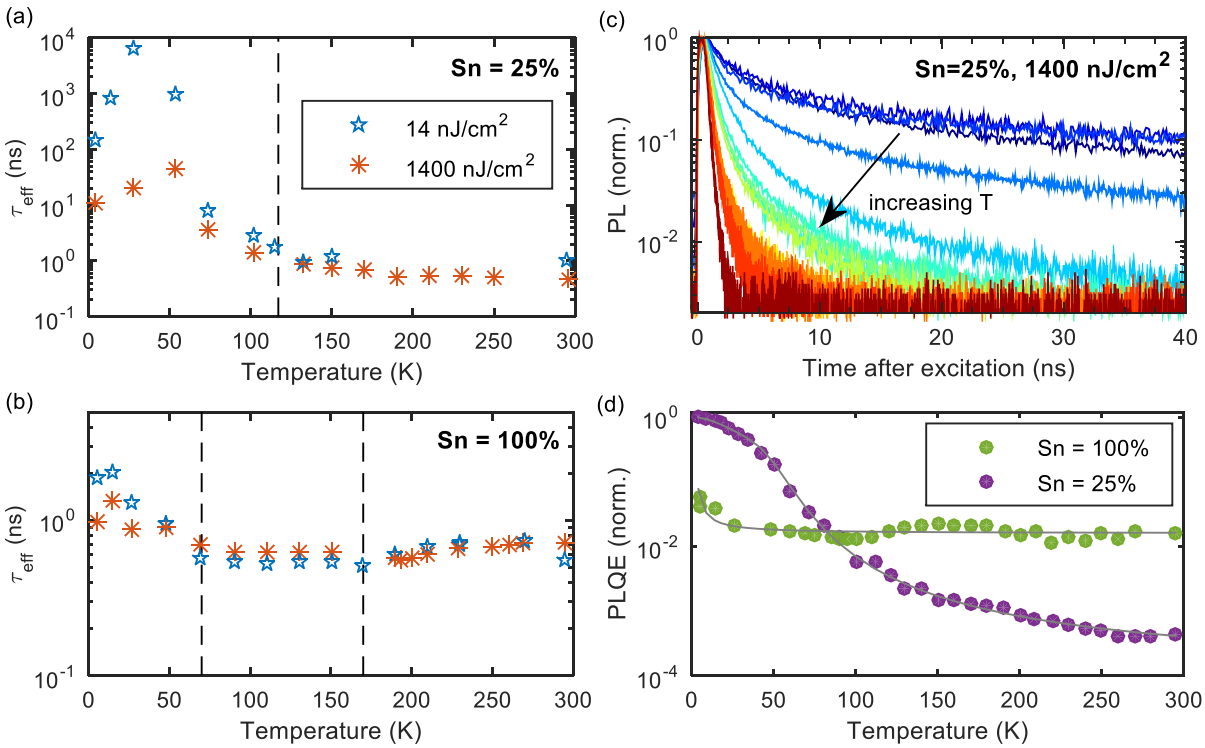

Figure 5. (a,b) Effective PL lifetime determined from stretched exponential fit for $FASn_xPb_{1-x}I_3$ with x=0.25 and 1, excited at 14 and 1400 nJ cm^{-2}. Phase transitions are shown by black dashed lines. (c) Temperature dependent PL decay curves for x=0.25, excited at 400 nm with a pulse energy of 1400 nJ cm^{-2}. (d) Relative PL intensity for x=0.25 and x=1 when excited at 400 nm with a power of 1 W cm^{-2} pulsed at 80 MHz. . PLQE for x=1 is fixed relative to x=0.25 at 295 K from Fig S4a. The PLQE is normalized by setting the intensity of the 25% Sn composition at T=5 K to a PLQE of 1 and scaling all other data by the same factor. Grey lines are fits, shown here as guides to the eye and discussed in the SI.